AAAS
Ultrafast Science
Volume 2022, Article ID 9867028, 9 pages
https://doi.org/10.34133/2022/9867028

Ultrafast Science
A SCIENCE PARTNER JOURNAL

Research Article

Air-Laser-Based Standoff Coherent Raman Spectrometer

Yao Fu,[1] Jincheng Cao,[1] Kaoru Yamanouchi,[2] and Huailiang Xu[1,3]

[1]*State Key Laboratory of Integrated Optoelectronics, College of Electronic Science and Engineering, Jilin University, Changchun 130012, China*
[2]*Department of Chemistry, School of Science, The University of Tokyo, 7-3-1 Hongo, Bunkyo-ku, Tokyo 113-0033, Japan*
[3]*CAS Center for Excellence in Ultra-Intense Laser Science, Shanghai 201800, China*

Correspondence should be addressed to Kaoru Yamanouchi; kaoru@chem.s.u-tokyo.ac.jp and Huailiang Xu; huailiang@jlu.edu.cn

Received 18 May 2022; Accepted 11 July 2022; Published 3 August 2022

Among currently available optical spectroscopic methods, Raman spectroscopy has versatile application to investigation of dynamical processes of molecules leading to chemical changes in the gas and liquid phases. However, it is still a challenge to realize an ideal standoff coherent Raman spectrometer with which both high temporal resolution and high-frequency resolution can be achieved, so that one can remotely probe chemical species in real time with high temporal resolution while monitoring the populations in their respective rovibronic levels in the frequency domain with sufficiently high spectral resolution. In the present study, we construct an air-laser-based Raman spectrometer, in which near-infrared femtosecond (fs) laser pulses at 800 nm and cavity-free picosecond N_2^+ air-laser pulses at 391 nm generated by the filamentation induced by the fs laser pulses are simultaneously used, enabling us to generate a hybrid ps/fs laser source at a desired standoff position for standoff surveillance of chemical and biochemical species. With this prototype Raman spectrometer, we demonstrate that the temporal evolution of the electronic, vibrational, and rotational states of N_2^+ and the coupling processes of the rovibrational wave packet of N_2 molecules can be probed.

1. Introduction

Spectrometers have been one of the most indispensable analytical tools to investigate frequency-dependent light-matter interactions that lie at the heart of a vast number of fundamental researches in astronomy, physics, chemistry, and biology. This has led to the development of spectrometers with a variety of specifications such as the operation wavelengths, time-and-frequency resolutions, and size required in a variety of applications [1–4]. Chemical changes of molecules involve a variety of dynamical processes accompanied by the excitation of molecular rotations and vibrations, which can be probed by Raman scattering-based spectroscopic techniques with atomic spatial and femtosecond temporal resolution [5].

In the past few decades, a variety of approaches of vibrational Raman detections of chemical species have been developed to achieve high temporal resolution and high-frequency resolution such as femtosecond stimulated Raman scattering (FSRS) [6, 7] and hybrid femtosecond/picosecond coherent anti-Stokes Raman scattering (fs/ps CARS) technique [8–11]. These vibrational Raman spectroscopic techniques provide direct insight into the vibrational level structures of molecules with high-frequency resolution through a basic four-wave mixing process that is governed by the third-order nonlinear susceptibility $\chi^3(\omega)$ [11, 12]. Therefore, the intensity of the resultant coherent Raman signal can be described as $I(\omega) \propto |\{\chi^3(\omega)[E_S(\omega) \bigstar E_p(\omega)]\} \bigotimes E_{pr}(\omega)|^2$, where $\bigstar$ and $\bigotimes$ represent, respectively, the cross-correlation operator and the convolution operator, and $E_p(\omega)$, $E_S(\omega)$, and $E_{pr}(\omega)$ represent, respectively, the electric fields of the three waves serving as the pump, Stokes, and probe pulses to generate the fourth coherent vibrational Raman signals [10]. Therefore, a Raman spectroscopic measurement system by which we can achieve both the high temporal resolution and the high-frequency resolution is in most cases large in size and expensive. In addition, it is not easy to use such an apparatus for the Raman detections at a standoff position because of the difficulty in spatiotemporal overlapping of the multiple laser systems with different wavelengths. On the other hand, it has been reported that air lasing with a few ps pulse duration and sub-10 cm^{-1}

frequency resolution can be achieved remotely in the cavity-free scheme [13–20] and can be used as a light source in spectroscopic measurements inducing those in coherent Raman spectroscopy [21–24] as well as in distinguishing carbon isotopes of CO_2 [25]. For remote sensing applications, we can optimize the energy of the air lasing and control the position in atmosphere where it is created in a manner that we reported before [26–28].

In the present study, we develop a standoff air-laser-based Raman spectrometer in which the intense fs near-IR pulsed laser and the ps 391 nm N_2^+ laser created by the filamentation of the fs laser are used in combination, and demonstrate the capability of the spectrometer for probing in real time a coherent rovibrational wave packet of molecules and molecular ions in the air by the coherent Raman scattering processes including resonant and nonresonant coherent Stokes Raman scattering (CSRS) and anti-Stokes Raman scattering (CARS). In this spectroscopic scheme, the ps-pulsed N_2^+ laser acts as a Raman pump to interact with a coherent rovibrational wave packet of molecules and molecular ions created in the air by the fs pulsed laser at a desired standoff distance by varying the focal position, that is, the interaction position. By varying the temporal delay between the ps pump and fs activation laser pulses, the temporal evolution of the rovibrational wave packet of molecules and molecular ions is probed in real time. To the best of our knowledge, this is the first demonstration of an air-laser-based standoff Raman spectrometer with sufficiently high temporal and high-frequency resolutions. Because this characteristic and advantageous performance of the air-laser-based coherent Raman technique can be realized by the nonlinear propagation of intense NIR femtosecond laser pulses in the air, the unique spectrometer device is promising to achieve remote sensing of chemicals and pollutants in the air and, thus, has a variety of potential applications not only in fundamental molecular science but also in environmental science.

2. Basic Principle and Methods

2.1. Principle and Design of the Standoff Air-Laser Raman Spectrometer. The standoff Raman spectrometer is composed of the hybrid air-laser-based fs/ps pulsed lasers, generated at a desired free-space position for the standoff detection of chemical species. The roles of the hybrid laser pulses in the Raman spectrometer are schematically shown in Figure 1(a). The broadband fs laser pulse whose bandwidth covers the frequencies, ω_1 and ω_2, initiates rotational and vibrational coherences in the electronic ground state of molecular species of interest, thereafter called "a fs activation pulse." The rotational and vibrational wave packets of the system are probed after a time delay Δt by the narrowband ps air-laser pulse, having the central frequency of ω_3, that drives the Raman transitions by the CSRS/CARS processes, thereafter called "a ps pump pulse." In our case, the fs laser pulse covers a broad spectral range of 710–840 nm with a pulse duration of ~60 fs, which is slightly chirped during the propagation in the air, and the ps pump pulse has the narrow bandwidth of ~5 cm^{-1} and the pulse duration of ~1.2 ps. The narrow bandwidth of the pump laser guarantees the high spectral resolution of the standoff Raman spectrometer. The layout of the spectrometer is schematically shown in Figure 1(b). The zero delay is defined as the timing when the activation pulse is temporally overlapped with the ps pump pulse, and the positive delay means that the activation pulse arrives the interaction zone before the ps pump pulse.

2.2. Methods. The air-laser Raman spectrometer was constructed based on a commercial Ti:sapphire laser system (Spectra Physics, Spitfire ACE) that produces intense ultrashort near-IR laser pulses (800 nm, 50 fs, 7.8 mJ/pulse, 200 Hz). The output of the laser system was split into two beams by a 9 : 1 beam splitter. The stronger beam (6.9 mJ/pulse) was focused by a lens (L1) (f = 400 mm) into a chamber filled with a nitrogen gas at 20 mbar to generate population-inverted N_2^+. The weaker beam was converted into second-order harmonic pulses (400 nm, 500 nJ/pulse) by a 200 μm β-barium borate (BBO) crystal. The generated UV pulses acted as seed light to be amplified in the chamber, producing N_2^+ lasing at 391 nm. After passing through the chamber, the forwardly propagating pulses were first collimated by a lens (L2) (f = 400 mm) and then separated by a dichroic mirror (DM1) with a high reflectivity at 800 nm and a high transmittance in the ultraviolet-visible wavelength range. The generated N_2^+ laser (391 nm) having a narrow bandwidth of ~5 cm^{-1} and a pulse duration of ~1.2 ps (see Figure 2(b)) was isolated from the seed light (400 nm) by a band-pass filter (F1) with the transmission center wavelength of 390 nm and the bandwidth of 10 nm. The near-IR laser pulses (800 nm, 4.5 mJ/pulse), slightly chirped by the filamentation process and the propagation through the chamber so that the pulse duration is stretched to ~60 fs and the spectral range is broadened to 710–840 nm (see Figure 2(b)), were reflected by DM1 and were purified by a long-pass (>532 nm) filter (F2), and then, combined collinearly with the 391 nm laser pulses using another polished dichroic mirror (DM2) with a high reflectivity at 800 nm and a high transmission in the ultraviolet-visible wavelength region. The delay time between the 800 nm laser pulse and the 391 nm laser pulse was varied using a delay line (Thorlabs MT1-Z8) inserted in the beam path for the 800 nm laser pulses, which provides a minimum time delay step of 0.33 fs between the 800 nm activation laser pulse and the 391 nm Raman pump pulse. However, the time delay step was set to be 300 fs in the present study in order to record the Raman signals in the wide temporal range of 45 ps.

The spectrum of the 391 nm laser pulses is shown in Figure 1(b), which was measured after removing the D4 damper and inserting an attenuator before the spectrometer (Shamrock 303i, Andor). The spectrum of the 800 nm laser pulses is also shown in Figure 1(b), which was measured by dispersing the light of the 800 nm laser pulses scattered at a paper by a fiber spectrometer (HR4000, Ocean Optics). The pulse width of the 391 nm laser pulses was determined to be ~1.2 ps by the cross-correlation trace shown in the inset of Figure 1(b), which was recorded as the intensity variation of the sum-frequency pulses generated at a BBO

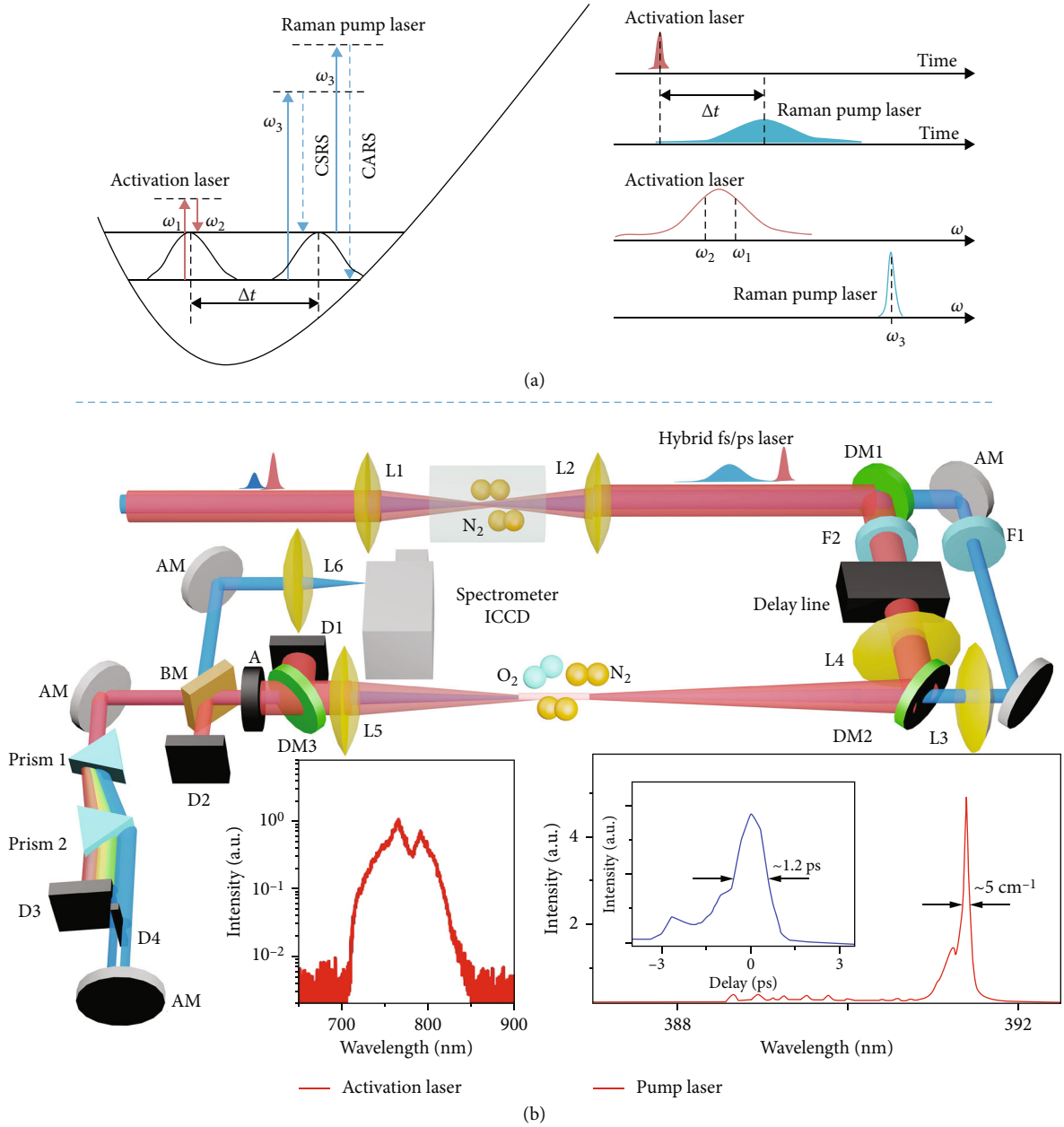

FIGURE 1: Concept and schematic of air-laser-based Raman spectrometer: (a) a typical energy-level diagram of diatomic molecules and diatomic molecular ions studied in the present study, N_2, O_2, and N_2^+, and the Raman activation and excitation schemes for the air-laser-based Raman spectrometer; (b) schematic of the air-laser-based Raman spectrometer and the spectrum of the fs activation pulse and the spectrum of the ps pump laser pulse generated by the filamentation of the fs laser pulse with its temporal shape (inset).

crystal (500 μm thickness) by the 391 nm laser pulses and the 800 nm laser pulses attenuated to 300 μJ/pulse as a function of the delay between the two pulses. The zero delay is defined as the timing when the 800 nm pulse is temporally overlapped with the 391 nm laser pulse, and the positive delay means that the 800 nm pulse arrives at the interaction point before the 391 nm laser pulse.

The 391 nm laser pulses, serving as the ps pump laser pulses, and the 800 nm laser pulses, serving as the fs activation laser pulses, were focused, respectively, by the L3 ($f = 1$ m) and L4 ($f = 1$ m) lenses. After passing through the focus, the laser beam was collimated by a lens (L5) ($f = 750$ mm) and the 800 nm component of the laser beam was reflected by a dichroic mirror (DM3). After passing through DM3, the laser beam was split into two by a 1 : 1 beam splitter (BM) (250–450 nm) and the laser beam passing through BM was dispersed by two prisms so that the supercontinuum and coherent Raman scattering light generated at the focus as well as the 391 nm laser beam were spatially separated, and finally, the supercontinuum in the visible range was blocked by a damper (D3). In addition, a metal strip damper (D4) was placed in the beam path, by which only the 391 nm laser beam was blocked, and the CSRS/CARS signals on the right and left spectral sides of

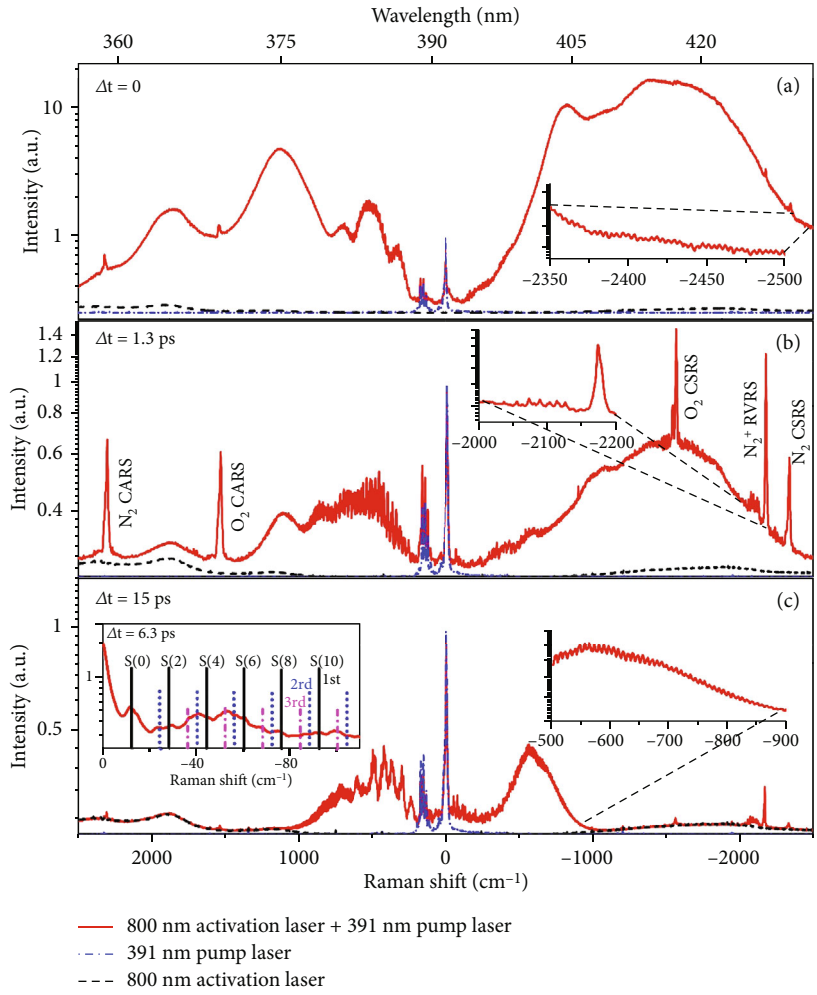

FIGURE 2: Comprehensive air-laser Raman spectra. Raman spectra measured in the spectral range between -2500 and 2500 cm^{-1} recorded by the fs activation laser only (black dash line), the ps pump laser only (blue dashed-dotted line), and the fs activation laser and ps pump laser (red solid line) at the delay times of (a) 0 ps, (b) 1.3 ps, and (c) 15 ps. The left-side inset in (c) indicates the spectral assignment of the sequential rotational CSRS at the head of the S-branch band of N_2 measured at the delay of $\Delta t = 6.3$ ps for the first (black solid), second (blue dash), and third (pink dash dot) orders of the S-branch rotational Raman signals of N_2.

the 391 nm laser, which were not blocked by D4, were reflected backward by an aluminum mirror (AM) and were focused by a lens (L6) ($f = 6$ cm) into a spectrometer (Shamrock 303i, Andor) equipped with an ICCD (iStar, Andor). The slit width of the spectrometer was set to be at 200 μm, and the gate delay and gate width of the ICCD were set to be at −5 ns and 100 ns, respectively.

3. Results and Discussion

3.1. Air-Laser Raman Spectra. Figures 2(a)–2(c) show the spectra of air constituents measured with the fs activation laser- only (black dash line), the ps pump only (blue dashed-dotted line), and the fs activation and ps pump (red solid line) at the delay time of $\Delta t = 0$ ps, 1.3 ps, and 15 ps. The data were accumulated over 5000 laser shots to achieve a high signal-to-noise ratio as well as to reduce the influence induced by the shot-by-shot fluctuations in the activation laser parameters. It can be clearly seen in Figures 2(a)–2(c) that only when both the activation and pump laser pulses are employed, several sharp peaks and broad bands at both red and blue sides of the 391 nm pump laser are generated, indicating that the ps pump laser at 391 nm laser pulse generates the coherent Raman scattering processes originating from the coherent media prepared by the fs activation laser pulse. It should be noted that the pump laser spectrum (blue lines) at 391 nm is strongly suppressed by D4, so that the relative spectral intensities of the P and R branches become different from those shown in Figure 1(b). The sharp peaks can be assigned to the coherent vibrational Raman lines of the Q-branch transitions of O_2 at 1556 (11) cm^{-1} (CARS) and -1556 (7) cm^{-1} (CSRS) and those of N_2 at 2330 (13) cm^{-1} (CARS) and -2330 (4) cm^{-1} (CSRS), where the numbers in the parentheses are the uncertainties in the measurements. The maximum conversion efficiencies from the air-laser intensity to the vibrational Raman signals are estimated to be ~10^{-5} under the current experimental conditions.

In addition, the peak appearing at 427.8 nm, equivalently at the Raman shift of −2175 (3) cm^{-1}, corresponds to the

transition between the $B^2\Sigma_u^+(v'=0)$ and $X^2\Sigma_g^+(v''=1)$ states of N_2^+ and is assigned to the P-branch of the resonant vibrational Raman scattering (RVRS) of N_2^+ because the 391 nm pump laser is resonant with the transition between the electronic states of $B^2\Sigma_u^+(v'=0)$ and $X^2\Sigma_g^+(v''=0)$ states of N_2^+, enhancing the Stokes Raman scattering. The small peaks at the blue side of the 427.8 nm RVRS peak, shown in the inset of Figure 2(b), are originated from the vibrational Raman scattering of the R-branch of the $B^2\Sigma_u^+$ $(v'=0)$ and $X^2\Sigma_g^+(v''=0)$ transition [29]. The bandwidth at full-width at half-maximum of the RVRS of N_2^+ is 8 cm^{-1}, which is slightly narrower than that (~12 cm^{-1}) of the CARS and CSRS signals of N_2 and O_2 due to the existence of the resonantly coupled upper levels. The double resonance also leads to more significant vibrational Raman scattering for the R-branch pump laser in the RVRS of N_2^+ than in the CARS and CSRS of N_2 and O_2.

The broad bands (red solid line) shown in Figures 2(a)–2(c) are ascribed to both the sequential rotational Raman excited by the 391 nm pump pulse in a cascading manner [22] and the nonresonant CSRS and CARS (thereafter called nonresonant CRS) processes of the air molecules, whose intensities vary with the delay time in the full spectral range from -2500 cm^{-1} to 2500 cm^{-1}. The sequential rotational Raman scattering [22] can be seen more clearly as the peaks appearing on the top of the nonresonant continuum in the region of 0-1000 cm^{-1}. The left-side inset in Figure 2(c) indicates that the significant sequential rotational CSRS signals at the head of the S-branch band of N_2 can be assigned to the first, second, and third orders of the rotational Raman signals of the S-branch ($J \longrightarrow J+2$) of N_2, indicating that the sequential coherent rotational Raman signals mainly originate from N_2 molecules. In the nonresonant Raman scattering, many rotational and rovibrational levels coherently prepared by the fs activation pulse are involved (see Subsection 3.2). As shown in Figure 2(a), i.e., the spectrum measured at the delay of $\Delta t = 0$, where the activation laser overlaps with the peak of the 391 nm laser pulse, the nonresonant CRS are significantly enhanced, and sequential rotational Raman spectra (see the inset of Figure 2(a)) can reach -2500 cm^{-1}. At the delay of $\Delta t = 15$ ps (Figure 2(c)), the activation laser pulse arrives at the interaction region much earlier and does not overlap temporally with the ps pump pulse, and nonresonant CRS could not occur [11]. Therefore, the broadband Raman signals are only attributed to the sequential rotational Raman process. The typical sequential rotational Raman spectrum in the range of -900 to -500 cm^{-1} is shown in the right-side inset of Figure 2(c), exhibiting rotational Raman peaks in the wide energy range originating from the cascading rotational excitations [22].

3.2. Time-Dependent Raman Processes. We measured, as shown in Figure 3, the intensities of these three kinds of Raman processes, i.e., the nonresonant CRS in the range of 417-420 nm, corresponding to the Raman shift range between -1567 and -1738 cm^{-1} (blue dotted line), the vibrational CSRS/CARS of N_2 at ±2330 cm^{-1} (red dashed line/pink dashed-dotted line), and the RVRS of N_2^+ at -2175 cm^{-1} (black solid line), as a function of the delay time. It can be seen in Figure 3 that the temporal variation of the intensities of these three different kinds of Raman process is significantly different from each other. The time dependence of the intensity of the nonresonant CRS is close to the temporal pulse shape of the 391 nm laser (see Methods). That is, the maximum appears at $\Delta t = 0$, where the activation laser temporally overlaps with the peak of the ps pump laser pulse. The slight difference between the nonresonant plot and the temporal profile of the 391 nm Raman pump laser can be ascribed to the delayed Kerr response effect in air molecules originating from the rotational transitions induced by the 800 nm activation laser front, which may affect the nonresonant Raman signals produced by the interaction with the rear part of the activation laser. Differently from the nonresonant CRS, the signal of the CSRS/CARS of N_2 takes the maximum intensity at $\Delta t = 0.6$ ps, and the decay of the CSRS/CARS of N_2 is much slower than that of the nonresonant CRS. The decay of the RVRS signals of N_2^+ is the slowest, and the signal of the RVRS signals of N_2^+ takes a maximum at the delay of 1.3 ps, which is latest among these three different Raman processes.

In order to understand the mechanisms of the generations of these Raman signals recorded by our spectrometer, i.e., the broadband nonresonant CRS, the vibrational CSRS/CARS of N_2, and the RVRS of N_2^+, we show the schematic energy-level diagrams in Figures 3(b)–3(e). The intensity of the coherent Raman signals is proportional to $|P^{(3)}(\omega)|^2$, in which $P^{(3)}(\omega)$ represents the third-order polarization and can be described as [11]

$$P^{(3)}(\omega) = P^{(3)}_{\mathrm{NR}}(\omega) + P^{(3)}_{\mathrm{R}}(\omega), \tag{1}$$

where $P^{(3)}_{\mathrm{NR}}(\omega)$ is the nonresonant component, which can be written as

$$P^{(3)}_{\mathrm{NR}}(\omega) = \int_0^{+\infty} d\Omega \times \chi^{(3)}_{\mathrm{NR}} \times E_3(\omega \pm \Omega) \times S_{12}(\Omega), \tag{2}$$

where Ω denotes the frequency difference between the two electric-field amplitudes, $E_1(\omega)$ and $E_2(\omega)$, contributing to the Raman scattering process within the bandwidth of the broadband activation laser, and $S_{12}(\Omega)$ denotes the convolution of $E_1(\omega)$ and $E_2(\omega)$, which can be written as

$$S_{12}(\Omega) \equiv \int_0^{+\infty} d\omega' \times E_1\left(\omega'\right) E_2^*\left(\omega' - \Omega\right), \tag{3}$$

$E_3(\omega)$ represents the electric field amplitude of the narrow-band ps pump laser; $\chi^{(3)}_{\mathrm{NR}}$ represents the "nonresonant" third-order susceptibility, which is usually insensitive to the frequency and can be assumed to be constant [11]. Therefore, the nonresonant contribution induces a smooth broadband spectral profile inherited from the $S_{12}(\Omega)$ as

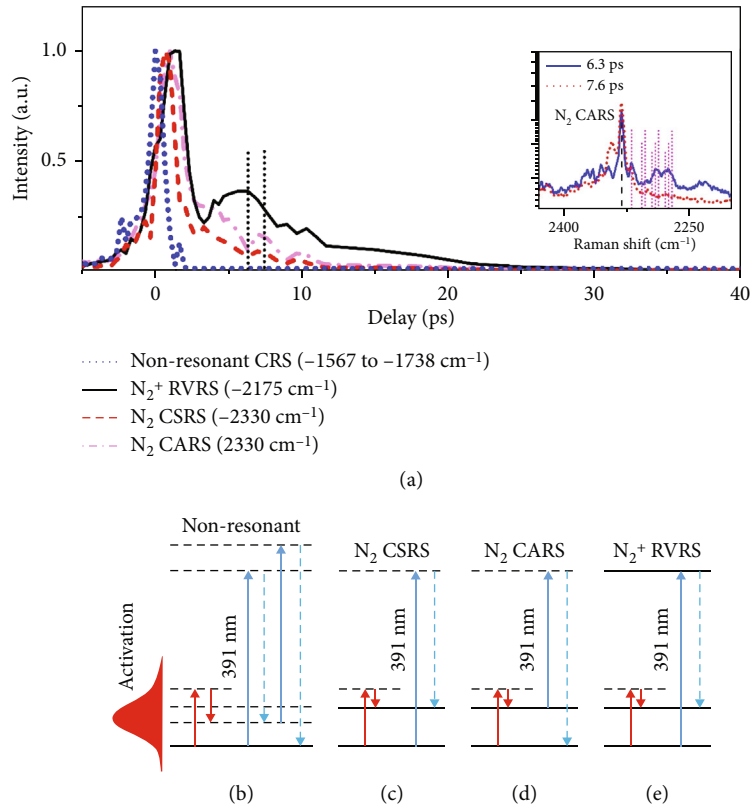

FIGURE 3: Time-dependent Raman processes. (a) The delay time dependences of the nonresonant CRS (blue dotted line) of N_2, the CSRS (red dashed line) of N_2, the CARS (pink dashed-dotted line) of N_2, and the RVRS (black solid line) of N_2^+. (b–e) The energy-level diagrams of the "nonresonant" CRS of N_2 (b), the CSRS (c), and CARS (d) of N_2 and the RVRS of N_2^+ (e). The inset in (a) shows the CARS spectra of N_2 in the range of 2200-2430 cm^{-1} measured at the delay between the activation and Raman pump of $\Delta t = 6.3$ ps (blue solid line) and $\Delta t = 7.6$ ps (red dotted line).

shown in Figures 2(a) and 2(b), which may cover the spectral ranges of the vibrational and rotational transitions of the molecular species of interest in the present study. Because the nonresonant CRS processes are insensitive to the transition frequencies, their transition schemes can be expressed using the virtual levels in the electronic ground state as expressed by the energy level diagram in Figure 3(b) (virtual levels). The nonresonant CRS occurs only in the period during which the fs activation laser pulse and the ps pump laser pulses overlap temporally [9]. This is the reason why its delay curve follows the profile of the ps pump pulse in the time domain and takes the maximum value when the activation pulse temporally overlaps with the peak of the ps pump laser pulse.

In the resonant case, $P_R^{(3)}(\omega)$ becomes dominant and can be written as

$$P_R^{(3)}(\omega) = \int_0^{+\infty} d\Omega \times \chi_R^{(3)}(\Omega) \times E_3(\omega \pm \Omega) \times S_{12}(\Omega), \quad (4)$$

where $\chi_R^{(3)}$ represents the resonant three-order susceptibility. The vibrational CSRS/CARS of N_2 at $\pm 2330\,cm^{-1}$ can be attributed to the singly resonant case [12], in which the two coherent real vibrational states of N_2 that are populated by two photons whose frequency difference matches the separation of the two vibrational levels (see the energy level diagrams in Figures 3(c) and 3(d)). Therefore, $\chi_R^{(3)}$ can be written as

$$\chi_R^{(3)}[\omega = \omega_3 \pm (\omega_1 - \omega_2)] = \frac{a}{(\omega_1 - \omega_2 - \omega_v) + i\Gamma_v}, \quad (5)$$

where ω_1 and ω_2 represent the frequencies of the two photons provided by the fs activation laser pulse, and the ω_3 represents the frequency of the photon of the ps pump laser pulse. The coefficient a represents the strength of the single resonance which is independent of ω_1 and ω_2 because $\omega_1 - \omega_2$ is scanned over the Raman resonance, Γ_v represents the half-width of the vibrational Raman peak profile, and ω_v represents the vibrational frequency. It can be seen that the resonant susceptibility can be significantly enhanced when $\omega_1 - \omega_2 = \omega_v$. Because the decay profiles of N_2 CSRS/CARS are related to the dispersion of the wave packet of N_2 originating from the anharmonicity of the molecular potential energy curve and the rotation-vibration coupling [30], the N_2 CSRS/CARS can remain even after the activation laser pulse disappears. After $\Delta t = 1.6$ ps, the fs activation laser pulse and the ps pump laser pulse are temporally separated almost completely, and the intensity

of the CSRS/CARS of N_2 decreases as Δt increases, as shown in Figure 3(a), which can be ascribed to the dispersion of the vibrational wave packet originating from the anharmonicity of the molecular potential energy surface and rotation-vibration coupling [30].

The maximum intensity of the CSRS/CARS of N_2 appears at the delay of $\Delta t \sim 0.6$ ps. This is because, at the delay of 0 ps, the front part of the ps pump laser pulse arrives at the interaction zone before the fs activation laser pulse and the CSRS/CARS process cannot be induced efficiently. Therefore, the optimized CSRS/CARS intensities in the N_2^+-laser-based coherent Raman spectroscopy can be obtained when $0 < \Delta t < 1.6$ ps. Moreover, when the two pulses temporally overlap at $\Delta t = 0$ ps, the shading of the Q-branch head of the vibrational CSRS/CARS towards the higher frequency side develops significantly, and consequently, the Q-branching head cannot form the sharp peak profile at the rotational band origin.

Furthermore, it can be seen in Figure 3(a) that oscillation structures with a period of ~2 ps appear in the decaying tails of the CSRS and CARS curves for the delay range of 0-10 ps. To explore the origin of these oscillation structures, we show in the inset of Figure 3 the two CARS spectra of N_2 in the range of 2200-2430 cm^{-1} measured, respectively, when the delays between the activation and Raman pump were at $\Delta t = 6.3$ ps (blue solid line) and $\Delta t = 7.6$ ps (red dotted line), which correspond to the minimum and maximum intensities of the oscillation structures marked by the black dotted line in Figure 3(a). The inset of Figure 3(a) clearly shows that the vibrational Q-branch transition of N_2 at ~2330 cm^{-1} (marked by the black dashed line in the inset) is directly induced by the 391 nm pump laser. In addition, the second-order vibrational Q-branch transition of N_2 at the Raman shift range between ~2342 cm^{-1} and ~2390 cm^{-1} (marked by the pink dotted lines in the inset) is observed and the rotational S-branch Raman laser of N_2 induced by the 391 nm pump laser is observed in the Raman shift range between ~12 cm^{-1} and ~60 cm^{-1}. This is confirmed by the comparison of the Raman shifts in the peaks in the inset of Figure 3(a) with those shown in the left-side inset of Figure 2(c). Therefore, the oscillation structures appearing in the CSRS and CARS signals shown in Figure 3(a) can be ascribed to the intensity variation in the 391 nm pump laser modulated by the rotation of N_2 with a quarter period of ~2 ps, resulting in the energy transfer from the 391 nm pump laser to the sequential rotational Raman laser.

For the RVRS of N_2^+ at -2175 cm^{-1}, it can be seen from the energy diagram shown in Figure 3(e) that, besides the two low-lying vibrational levels, the coherent vibrational Raman transition consists of a one-photon resonant electronic transition, which can be interpreted by the doubly resonant cases [12]. Therefore, $\chi_R^{(3)}$ can be written as

$$\chi_R^{(3)}[\omega = \omega_3 - (\omega_1 - \omega_2)] = \frac{b}{[(\omega_1 - \omega_2 - \omega_v) + i\Gamma_v][(\omega_3 - \omega_1 + \omega_2 - \omega_e) + i\Gamma_e]}, \quad (6)$$

where b represents the strength of the double resonance. Γ_v and Γ_e represent, respectively, the half-widths of the vibrational and electronic transition peak profiles and ω_v and ω_e represent, respectively, the frequencies corresponding to the vibrational and electronic transitions.

After the multiphoton/tunnel ionization of N_2 by the fs activation laser, the coherence of the two vibrational states, i.e., the $X^2\Sigma_g^+(v'' = 1)$ and $X^2\Sigma_g^+(v'' = 0)$ states of N_2^+, is prepared. In addition, the rear part of the spectrally broadened fs activation pulse can also contribute to the creation of the coherence of the two vibrational levels. The ps pump laser which is resonant with the electronic transition between the $B^2\Sigma_u^+(v' = 0)$ and $X^2\Sigma_g^+(v'' = 0)$ states induces the RVRS process. The decay time of the RVRS of N_2^+ is much longer than that of CSRS/CARS of N_2, which may be attributed to the smaller dispersion in the vibrational wave packet of N_2^+.

In addition, the maximum of the RVRS appears at $\Delta t = 1.3$ ps, which is later than that of the nonresonant CRS and CSRS/CARS. This may be ascribed to the fact that the ps pump laser is electronically resonant with the $B^2\Sigma_u^+(v' = 0) - X^2\Sigma_g^+(v'' = 0)$ transition. Because the dispersion of the vibrational wave packet originates from the anharmonicity of the molecular potential energy curve and rotation-vibration coupling [30], the decay of RVRS reveals the temporal evolution of the electronic, vibrational, and rotational states of N_2^+.

4. Conclusion

In summary, by introducing the Raman spectroscopic signatures of the atmospheric constituents, we have demonstrated that our spectrometer provides simultaneous standoff detections of the coherent resonant and nonresonant rotational and vibrational Raman processes of molecules with the high temporal resolution and the high-frequency resolution. The key advantages of this technique originate from the ps pump laser generated by the filamentation created by the intense fs pulsed laser in the atmosphere, producing the hybrid air-laser-based ps/fs laser pulses at a desired free-space position. We have conducted a proof-of-principle demonstration of our spectrometer by the observation of the temporal evolution of the rovibrational wave packet of N_2 as well as by the observation of the temporal evolution of the electronic, vibrational, and rotational wave packet of N_2^+. This air-laser-based coherent Raman technique with high-frequency resolution and high temporal resolution can easily be implemented in standoff spectroscopy for remote sensing of chemicals and pollutants in the air. In conclusion, the concept of this standoff air-laser Raman spectrometer opens new opportunities for researchers to explore remote detection and surveillance of chemical and biochemical species with sufficiently high temporal and high-frequency resolutions.

Data Availability

The data that support the plots within this article and other findings of this study are available from the corresponding author upon reasonable request.

Conflicts of Interest

The authors declare that there is no conflict of interest regarding the publication of this article.

Authors' Contributions

H. L. X. and K.Y. developed the concept and designed the experiment. Y. F., J. C. C., and H.L.X. performed the experiments. Y. F., J. C. C., K. Y., and H. L. X. analyzed the data. The manuscript was prepared by Y. F., K. Y., and H. L. X. and was discussed among all authors.

Acknowledgments

The work is supported in part by the National Natural Science Foundation of China (NSFC) (62027822) and Japan Society for the Promotion of Science KAKENHI Grants (15H05696 and 20H00371).

References

[1] C. P. Bacon, Y. Mattley, and R. DeFrece, "Miniature spectroscopic instrumentation: applications to biology and chemistry," *Review of Scientific Instruments*, vol. 75, no. 1, pp. 1–16, 2004.

[2] Z. Y. Yang, T. Albrow-Owen, W. W. Cai, and T. Hasan, "Miniaturization of optical spectrometers," *Science*, vol. 371, no. 6528, article eabe0722, 2021.

[3] E. Le Coarer, S. Blaize, P. Benech et al., "Wavelength-scale stationary-wave integrated Fourier-transform spectrometry," *Nature Photonics*, vol. 1, no. 8, pp. 473–478, 2007.

[4] Z. Yang, T. Albrow-Owen, H. Cui et al., "Single-nanowire spectrometers," *Science*, vol. 365, no. 6457, pp. 1017–1020, 2019.

[5] E. T. J. Nibbering, H. Fidder, and E. Pines, "Ultrafast chemistry: using time-resolved vibrational spectroscopy for interrogation of structural dynamics," *Annual Review of Physical Chemistry*, vol. 56, no. 1, pp. 337–367, 2005.

[6] C. Fang, R. R. Frontiera, R. Tran, and R. A. Mathies, "Mapping GFP structure evolution during proton transfer with femtosecond Raman spectroscopy," *Nature*, vol. 462, no. 7270, pp. 200–204, 2009.

[7] P. Kukura, D. W. McCamant, S. Yoon, D. B. Wandschneider, and R. A. Mathies, "Structural observation of the primary isomerization in vision with femtosecond-stimulated Raman," *Science*, vol. 310, no. 5750, pp. 1006–1009, 2005.

[8] B. D. Prince, A. Chakraborty, B. M. Prince, and H. U. Stauffer, "Development of simultaneous frequency- and time-resolved coherent anti-Stokes Raman scattering for ultrafast detection of molecular Raman spectra," *The Journal of Chemical Physics*, vol. 125, no. 4, p. 044502, 2006.

[9] H. U. Stauffer, J. D. Miller, M. N. Slipchenko et al., "Time- and frequency-dependent model of time-resolved coherent anti-Stokes Raman scattering (CARS) with a picosecond-duration probe pulse," *The Journal of Chemical Physics*, vol. 140, no. 2, p. 024316, 2014.

[10] C. H. Camp Jr., Y. J. Lee, J. M. Heddleston et al., "High-speed coherent Raman fingerprint imaging of biological tissues," *Nature Photonics*, vol. 8, no. 8, pp. 627–634, 2014.

[11] D. Pestov, R. K. Murawski, G. O. Ariunbold et al., "Optimizing the laser-pulse configuration for coherent Raman spectroscopy," *Science*, vol. 316, no. 5822, pp. 265–268, 2007.

[12] Y. R. Shen, *The Principles of Nonlinear Optics*, Wiley, New York, 1984.

[13] Q. Luo, W. Liu, and S. L. Chin, "Lasing action in air induced by ultra-fast laser filamentation," *Applied Physics B: Lasers and Optics*, vol. 76, no. 3, pp. 337–340, 2003.

[14] A. Dogariu, J. B. Michael, M. O. Scully, and R. B. Miles, "High-gain backward lasing in air," *Science*, vol. 331, no. 6016, pp. 442–445, 2011.

[15] J. Yao, B. Zeng, H. Xu et al., "High-brightness switchable multiwavelength remote laser in air," *Physical Review A*, vol. 84, no. 5, article 051802, 2011.

[16] H. Li, D. Yao, S. Wang, Y. Fu, and H. Xu, "Air lasing: phenomena and mechanisms," *Chinese Physics B*, vol. 28, no. 11, p. 114204, 2019.

[17] M. Richter, M. Lytova, F. Morales et al., "Rotational quantum beat lasing without inversion," *Optica*, vol. 7, no. 6, pp. 586–592, 2020.

[18] Y. Liu, P. Ding, G. Lambert, A. Houard, V. Tikhonchuk, and A. Mysyrowicz, "Recollision-induced superradiance of ionized nitrogen molecules," *Physical Review Letters*, vol. 115, no. 13, 2015.

[19] J. Yao, S. Jiang, W. Chu et al., "Population redistribution among multiple electronic states of molecular nitrogenions in strong laser fields," *Physical Review Letters*, vol. 116, no. 14, 2016.

[20] H. Xu, E. Lotstedt, A. Iwasaki, and K. Yamanouchi, "Sub-10-fs population inversion in N_2^+ in air lasing through multiple state coupling," *Nature Communications*, vol. 6, no. 1, p. 8347, 2015.

[21] J. Ni, W. Chu, H. Zhang et al., "Impulsive rotational Raman scattering of N_2 by a remote "air laser" in femtosecond laser filament," *Optics Letters*, vol. 39, no. 8, pp. 2250–2253, 2014.

[22] Z. Liu, J. Yao, H. Zhang et al., "Extremely nonlinear Raman interaction of an ultrashort nitrogen ion laser with an impulsively excited molecular wave packet," *Physical Review A*, vol. 101, no. 4, 2020.

[23] X. Zhao, S. Nolte, and R. Ackermann, "Lasing of N_2^+ induced by filamentation in air as a probe for femtosecond coherent anti-Stokes Raman scattering," *Optics Letters*, vol. 45, no. 13, pp. 3661–3664, 2020.

[24] F. Zhang, H. Xie, L. Yuan et al., "Background-free single-beam coherent Raman spectroscopy assisted by air lasing," *Optics Letters*, vol. 47, no. 3, pp. 481–484, 2022.

[25] Z. Zhang, F. Zhang, B. Xu et al., "High-sensitivity gas detection with air-lasing-assisted coherent Raman spectroscopy," *Ultrafast Science*, vol. 2022, article 9761458, 2022.

[26] H. Li, M. Hou, H. Zang et al., "Significant enhancement of N_2^+ lasing by polarization-modulated ultrashort laser pulses," *Physical Review Letters*, vol. 122, no. 1, article 013202, 2019.

[27] H. Li, E. Lötstedt, H. Li et al., "Giant enhancement of air lasing by complete population inversion in N_2^+," *Physical Review Letters*, vol. 125, article 053201, no. 5, 2020.

[28] Y. Fu, J. Cao, S. Wang et al., "Extremely enhanced N_2^+lasing in a filamentary plasma grating in ambient air," *Optics Letters*, vol. 46, no. 14, pp. 3404–3407, 2021.

[29] H. Zhang, C. Jing, J. Yao et al., "Rotational coherence encoded in an "air-laser" spectrum of nitrogen molecular ions in an intense laser field," *Physical Review X*, vol. 3, no. 4, 2013.

[30] J. H. Odhner, D. A. Romanov, and R. J. Levis, "Wave-packet dispersion during femtosecond laser filamentation in air," *Physical Review Letters*, vol. 103, no. 7, 2009.